3D printing non-assembly compliant joints for soft robotics

Ali Zolfagharian [a,*], Mohammad Lakhi [a], Sadegh Ranjbar [b], Yonas Tadesse [c], Mahdi Bodaghi [d]

[a] *School of Engineering, Deakin University, Geelong, Victoria, 3216, Australia*
[b] *Department of Mechanical Engineering, Urmia University, Urmia, Iran*
[c] *Humanoid, Biorobotics and Smart Systems (HBS) Laboratory, Department of Mechanical Engineering, The University of Texas at Dallas, USA*
[d] *Department of Engineering, School of Science and Technology, Nottingham Trent University, Nottingham, NG11 8NS, UK*

ARTICLE INFO

ABSTRACT

This paper investigates integrating non-assembly three-dimensional (3D)-printed joints and soft robotic muscles in order to make a tendon-driven robotic finger. A finger-type structure actuated by electro-thermal soft actuator mechanism is introduced, including a bio-inspired 3D-printed compliant joint. As an affordable but high-performance component, twisted and coiled polymer (TCP) is used to drive the system as an actuator. The Euler–Lagrangian method and a transfer function based on an electro-thermo-mechanical model are used to analyze finger joints. The compliant joints are non-assembly 3D-printed spiral springs with high customization capabilities incorporated into the model. The simulation analysis is conducted to elucidate how the electro-thermal muscle and the spiral spring joint properties influence the finger motion. The results reveal further understanding of the 3D-printed spiral spring joints effects on the behavior of the soft robotic limbs. The suggested method can be adapted and employed in a broad variety of medicinal and industrial applications.

1. Introduction

When it comes to handling delicate goods, soft grippers are new inventions that may well be employed in contact with live tissues, human organs, and agriculture or foodstuffs without damaging their skins [1–3]. Soft grippers' conformal nature to grasp items of varying geometries and stiffness under uniform force is provided by soft materials utilized in these devices [4,5]. However, these grippers have high degrees of freedom (DOF), which increases their complexity of control [6–8]. That is where compliant mechanisms could be developed to solve these problems [9–11].

Pneumatics or hydraulics are typically used to operate the soft grippers, necessitating complicated systems and components [12]. Compliant grippers that are powered by tendons may be made in a single piece utilizing three-dimensional (3D) printing of polymers [13], which reduces the number of components and complexity in the system while providing constant grip force input and output [14]. Unique soft grippers for a range of uses might be produced at a lower cost with fused deposition modelling (FDM), which is one of the most cost-effective 3D printing processes [4]. There are fewer components in the non-assembly 3D-printed soft gripper compared to the rigid ones used in traditional production, resulting in decreased manufacturing and assembly times

and, ultimately, lower costs and fewer processing prone faults [15–17]. The compliant 3D-printed mechanisms are designed for less computational control effort and customized design [18,19], mechanical advantage [20] in medical soft robotic application [4,21].

Using a compliant mechanism in these applications has the benefits of small size, low power consumption, and simple control algorithms [22]. Many robotics and wearable system applications are constrained by the size and weight of variable stiffness compliant mechanisms [23]. Because of its ability to economically house longer lengths of beams inspired by the spiral form in mammalian cochlea, the spiral mechanism has been chosen among many different types of geometrical shapes to model the flexural beams [23,24]. 3D printing, and recently four-dimensional (4D) printing, has made use of spiral springs because of its space-saving design and unique twist deformation properties [25]. These springs have the potential to store a large amount of elastic energy in a small volume, making them both lighter and smaller in size [25,26]. In addition, spiral spring motion is used in soft gripper joints to provide passive compliance and reduce impact impedance while preventing abrupt and unexpected motion behavior and contact-induced vibration [27,28].

There have been few works recently investigated the integration of compliant joints into soft robotic applications. A human like finger with

---

* Corresponding author.
    E-mail address: a.zolfagharian@deakin.edu.au (A. Zolfagharian).
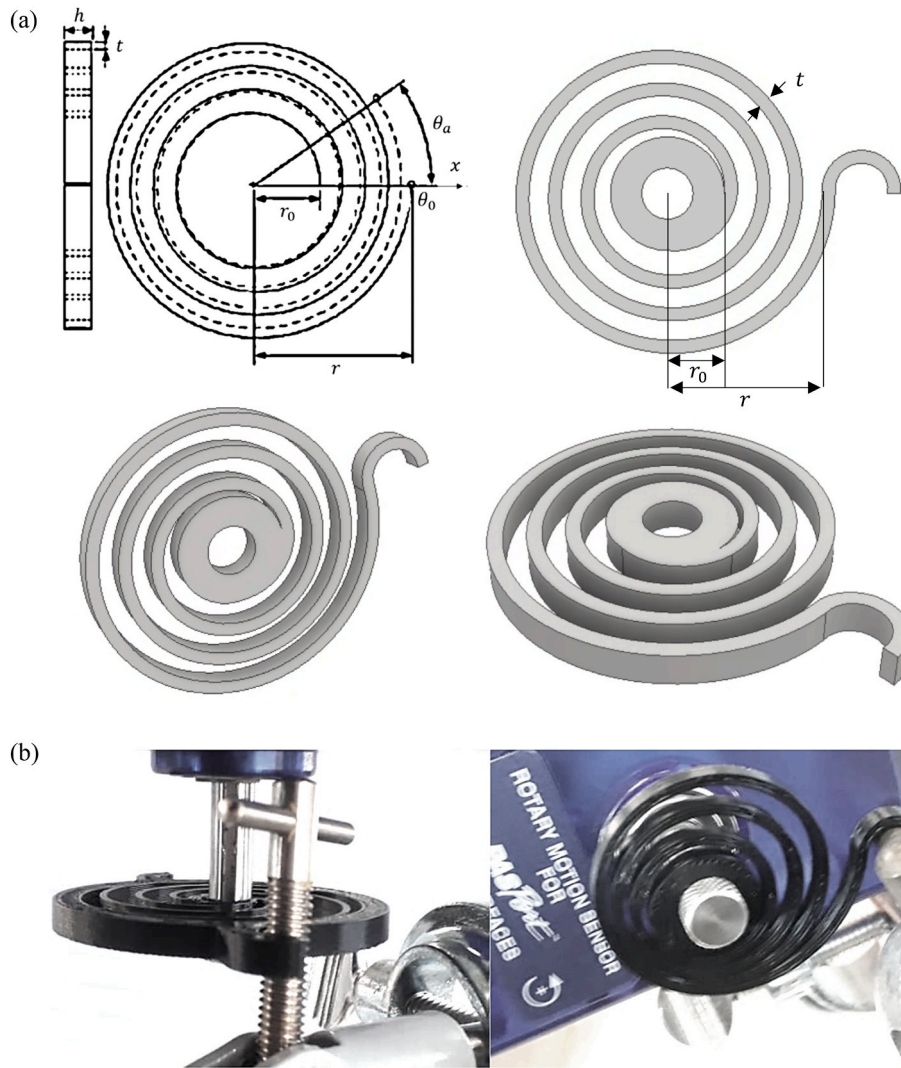
Fig. 1. (a) The geometry design and specification of 3D-printed spiral spring for initial testing from different views ($r_0 = 7mm$, $r = 19mm$, $t = 1.6mm$), (b) Sensory setup for force and angular position.

Table 1
Spiral spring joint 3D printing process parameters.

Printing Parameters	ABS	Nylon
Raster angle (○)	0	0
Infill percentage (%)	70	70
Nozzle speed (mm/s)	30	30
Nozzle temperature (○C)	200	250
Density (gr/cm³)	1.04	1.06
Layer thickness (mm)	0.25	0.25
Bed temperature (○C)	90	60

dual morphing through active/passive variable rigidity was developed using embedded conductive thermoplastic starch polymers in a pneumatic soft actuator. A dual stiffness mode was proposed to control the output force of the finger [29]. A bioinspired soft griper was developed using 3D printing and a linear actuator. The soft gripper was used for picking and placing a strawberry [30]. A bi-stable mechanism was also developed and experimentally tested for a controllable-compliance joint of an exoskeleton rehabilitation robot using a pneumatic actuator [31].

However, using the 3D printing manufacturing method to develop the product in the fewer steps and a non-assembly approach is quite novel, requiring further study. In this study, a non-assembly tendon-actuated soft robotic finger is designed and 3D-printed, utilizing

bioinspired spiral springs to create the appropriate force and motion while reducing the device's price and complexity. The rest of the paper is organized as follows. The methodology for designing and modeling the soft robotic finger actuators, including spiral spring design, system identification, and kinematic and dynamic models of the system, is described in Section 2 of this paper. Results from the soft robotic finger's simulation are shown in Section 3. The paper concludes in Section 4.

2. Methodology

2.1. 3D-printed spiral spring design and characterization

There are two things that might affect how much torque is needed to make a spiral spring: the spring geometry and the kind of material used to make it. Additive manufacturing (AM) technology was used to establish a technique for constructing spiral springs that took geometry, material, and predicted output characteristics, such as spring stiffness and size, into account [30,32]. The size of the springs is first determined, and then the materials and stiffness required are specified using 3D printing. Eq. (1), which describes the location of the end of a spiral, is used to construct the spiral spring as illustrated in Fig. 1b, where r is the distance from the centre of the spiral to the end point and r_0 is the spiral inner radius. $m = \frac{p}{2\pi}$, p is the pitch, distance between each coil of the
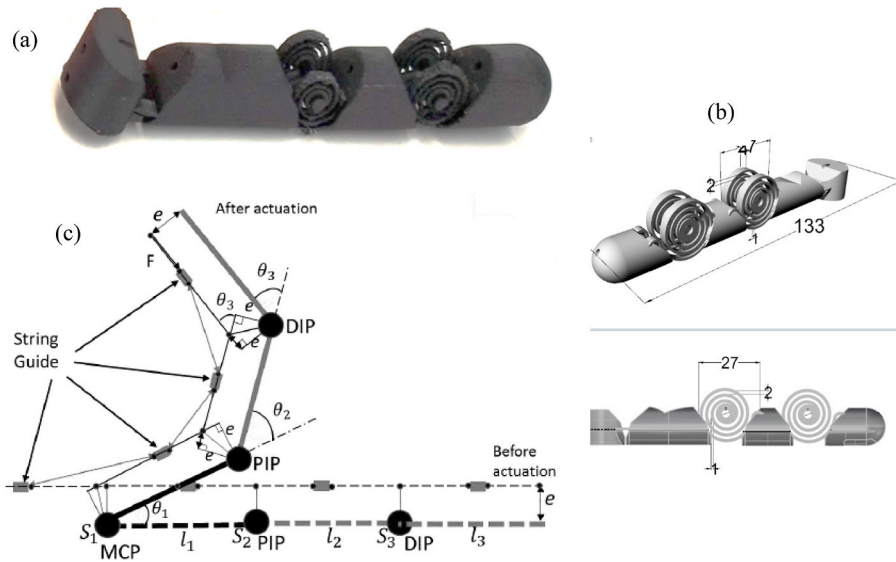
Fig. 2. (a) 3D-printed finger and spiral spring, (b) CAD model of the finger assembly, (c) free body diagram after actuation and before actuation of the tendon-muscle.

spiral; and the spiral twists angle θ [33] defined as:

$$r = m(\theta + \theta_0) + r_0 \tag{1}$$

θ_0 is s the counter-clockwise angle from the fixed point to the spiral's inner shaft to the x-axis., and the length of coil, L is expressed in Eq. (2) [34] where the length of spiral for three revolutions (6π) could be calculated as:

$$L = \int_0^L ds = \int_0^L \sqrt{(dr)^2 + (rd\theta)^2} = \int_0^{\theta_a} \sqrt{m^2 + r^2} d\theta. \tag{2}$$

The angular deflection of the spring is expressed as θ_a. The Castilian's Theorem [35] is also used to compute the strain angle as:

$$U = \int \frac{M^2 dx}{2EI} \tag{3}$$

in which E is the material's elastic modulus, the moment of inertia, I, and the torque of spring is represented as $M = Fr$. The spring end deformation angle is:

$$r\theta = \frac{\partial U}{\partial F} = \int_0^l \frac{\partial}{\partial F} \left(\frac{F^2 r^2 dx}{2EI} \right) = \int_0^l \frac{Fr^2}{EI} dx. \tag{4}$$

The spring coil has a rectangular cross-section with height and thickness of h and t, respectively, yields the following equation $I = \frac{ht^3}{12}$. Combining Eqs. (3) and (4) results in:

$$k = \frac{M}{d\theta} = \frac{Eht^3}{12L} \left(\frac{\pi}{180} \right). \tag{5}$$

The 3D printing material's Young's modulus used to fabricate the spring joint proportional to the moment output of the spring as derived in Eq. (5).

Taulman Nylon 645 and Formfutura Premium ABS were used here to create the 3D-printed springs. Table 1 provides more information on the 3D printing process, including the infill percentage as well as other processing factors and settings. Using tensile tests, the elastic modulus of ABS and nylon was found to be 1.607 GPa and 0.793 GPa, respectively. The stiffness of the 3D-printed joints was measured in accordance with an integrated system for measuring forces and angles, which included a PASCOE PASPort device (Fig. 1b). For this experiment, a threaded screw was used to secure the spring to one side of the angular sensor and

measure the necessary force to spin the wheel on the sensor.

2.2. Design and modeling of soft robotic finger actuator

The tendon-driven robotic finger (Fig. 2) actuated by electro-thermal muscles, using twisted and coiled polymer (TCP) muscles. When an external load is applied to the system, the system's energy changes, resulting in a linear stroke and creating a bending moment. For both electro-thermal (Fig. 3a) and ermss-mechanical (Fig. 3b) models, compared to the external load, the twisting moment is insignificant. A second-order electro-thermal transfer function (TF$_1$) was found a mean square error (MSE) of 8.39% for 90% accuracy, which can represent the model of TCP actuators.

$$TF_1 = \frac{-2.072s + 6.622}{s^2 + 2.112s + 0.1259} = \frac{T(s)}{P(s)} \tag{6a}$$

There was a first-order thermomechanical transfer function (TF2) with 93% accuracy (MSE, 0.001362). The TF2 is shown in the following:

$$TF_2 = \frac{0.02032s + 0.003318}{s + 0.2947} = \frac{F(s)}{T(s)} \tag{6b}$$

The system's electro-thermo-mechanical behavior was predicted using the coupled transfer functions in series. Simulink® was used to simulate the tendon-driven muscle's power input and force output. Fig. 3c shows the Simulink model that was used to compare and analyze the TFs. Understanding the molecular structure of polymeric precursor fibers led to the development of TCP muscles. These fibers are made up of polymeric chains that are quite flexible and aligned in the fiber direction. Due to their small constraint in non-crystalline area, these fibers exhibit large reversible contractions when heated, even if they have a minor negative thermal coefficient in the crystalline region. This principle yields a 4% strain for nylon 6 that is quite competitive with Ni–Ti SMA wires. Adding twist to the fiber also increases this effect, making it chiral.

The soft robotic finger is shown in Fig. 2 as three joints, which correspond to the distal, middle, and proximal phalanges. The velocity Jacobians of the index finger were calculated using a dynamic model based on the Euler-Lagrangian technique. For the tendon, the offset 'e' is 4.5 mm in length. The modeling method follows the one mentioned in Ref. [37]. To simulate the tendon-muscle dynamics, the following hypotheses are made: (1) tendon movement through guides is smooth because the tension is uniform along its length, (2) the 3D-printed
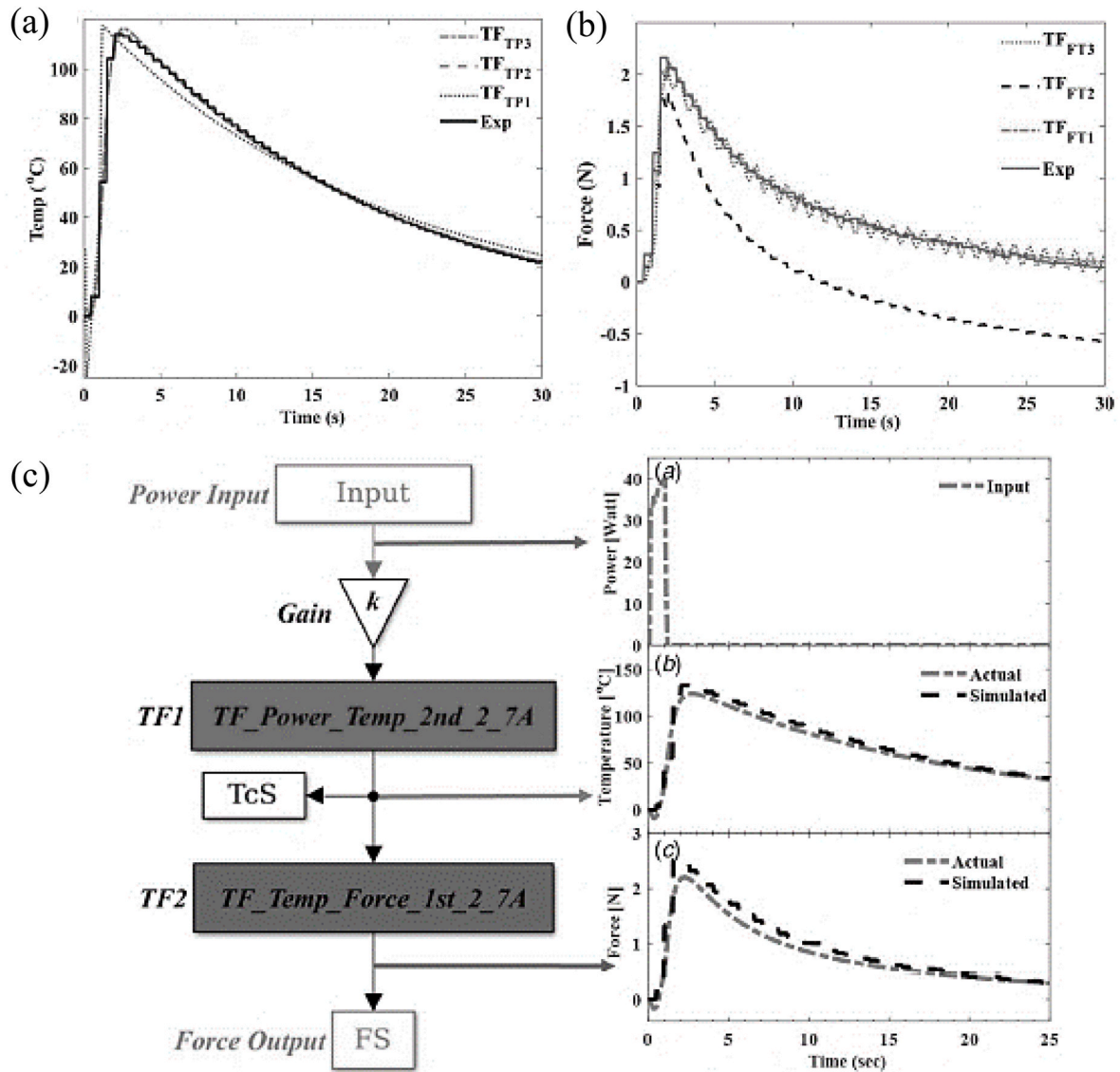
Fig. 3. Various order transfer functions for (a) electro-thermal systems, (b) thermos-mechanical systems, and (c) block diagram of the Simulink® model used for predicting the output behavior of the TCP muscle using the coupled transfer functions to relate the output force to electrical input [36].

Table 2
Simulation parameters of the soft robotic finger [36].

Parameter	Value
Simulation time	45 s (regular actuation)
Damping factor (C_d)	1×10^{-3} N ms.rad^{-1}
Mass of link 1 (m_1)	5.85×10^{-4} kg
Mass of link 2 (m_2)	4.50×10^{-4} kg
Mass of link 3 (m_3)	3.91×10^{-4} kg
Input force	3 N
Spring constant (theoretical)[a]	5.23×10^{-4} N m.deg^{-1}
Spring constant (exp. Mean) (K)	6.12×10^{-4} N m.deg^{-1}
Length of link 1 (l_1)	1.2×10^{-2} m
Length of link 2 (l_2)	9.0×10^{-3} m
Length of link 3 (l_3)	1.2×10^{-2} m
Offset distance I	4.5×10^{-3} m
Moment of inertia (i_1)	6.26×10^{-6} kg m^2
Moment of inertia (i_2)	5.55×10^{-6} kg m^2
Moment of inertia (i_3)	6.76×10^{-6} kg m^2

springs have identical properties, (3) the input force and temperature profiles of the actuator (the TCP muscle) are known beforehand to conducting experiments. Eq. (7) is a common one used for Euler-Lagrangian modeling.

$$\frac{d}{dt}\left(\frac{\partial K}{\partial \dot{q}_i}\right) - \left(\frac{\partial K}{\partial \dot{q}_i}\right) + \frac{\partial P}{\partial q_i} = \tau_i \quad (7)$$

K is the kinetic energy, P is the potential energy, and τ_i is the torque of the ith joint. After performing some mathematical operations and transformations, Eq. (7) may be expressed as:

$$\sum_j d_{kj}\ddot{q}_j + \sum_{ij}\left\{\frac{\partial d_{kj}}{\partial q_i} - \frac{1}{2}\frac{\partial d_{ij}}{\partial q_k}\right\}\dot{q}_i\dot{q}_j + \frac{\partial P}{\partial q_k} = \tau k \quad (8)$$

Expanding this equation for three linkages results in:

$$\tau_1 = d_{11}\ddot{q}_1 + d_{12}\ddot{q}_2 + d_{12}\dot{q}_2 + C_{111}\dot{q}_1^2 + C_{221}\dot{q}_2^2 + C_{331}\dot{q}_3^2 + (C_{111}+C_{121})\dot{q}_1\dot{q}_2$$
$$+ (C_{311}+C_{131})\dot{q}_3\dot{q}_1 + (C_{321}+C_{231})\dot{q}_2\dot{q}_3 + \varphi_1 + \tau_{d1}$$

$$(9a)$$

$$\tau_2 = d_{21}\ddot{q}_1 + d_{22}\ddot{q}_2 + d_{23}\dot{q}_3 + C_{112}\dot{q}_1^2 + C_{222}\dot{q}_2^2 + C_{332}\dot{q}_3^2 + (C_{212}+C_{122})\dot{q}_1\dot{q}_2$$
$$+ (C_{312}+C_{132})\dot{q}_3\dot{q}_1 + (C_{322}+C_{232})\dot{q}_2\dot{q}_3 + \varphi_1 + \tau_{d2}$$

$$(9b)$$
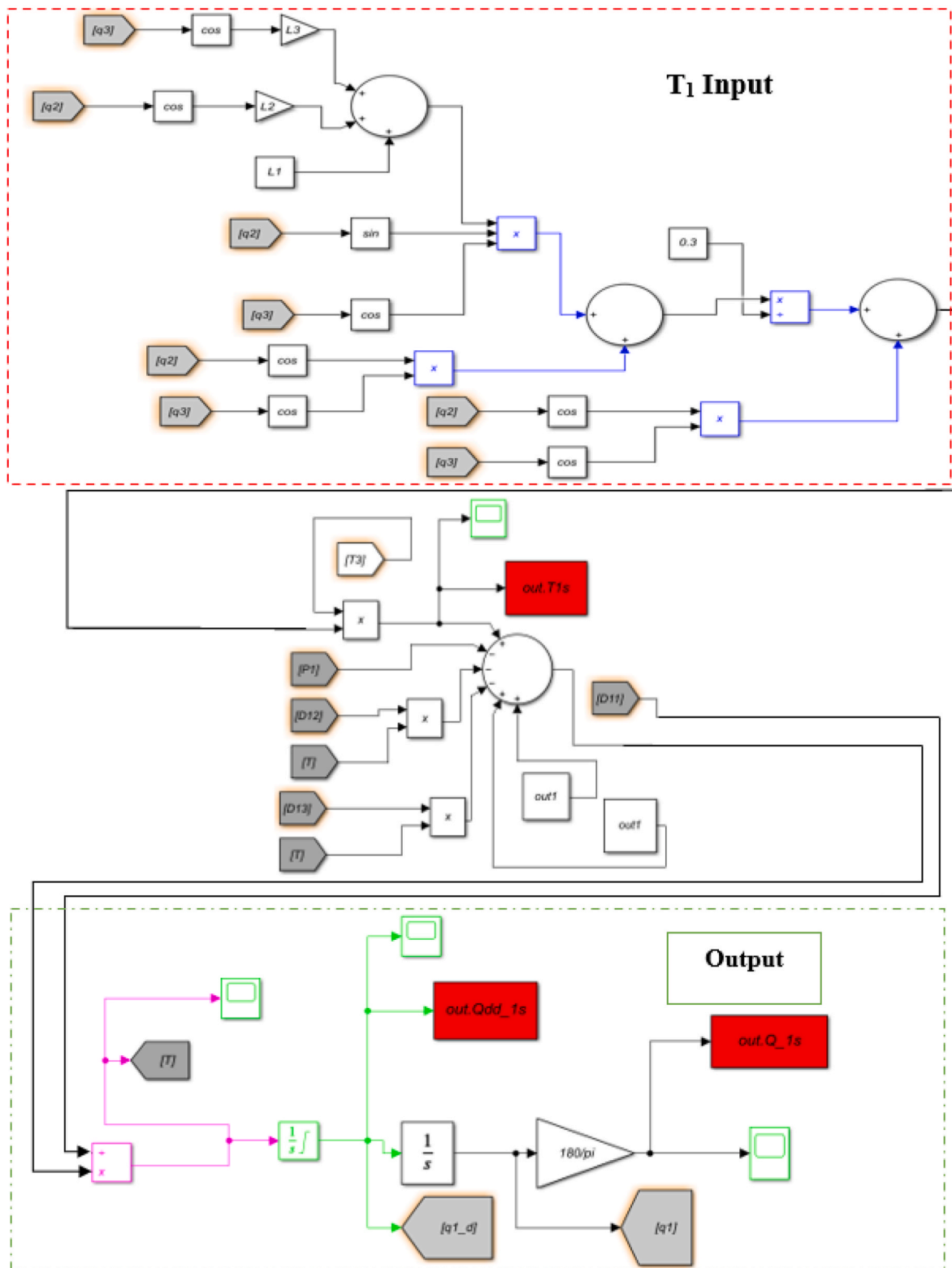
Fig. 4. Diagram of the Simulink model used to model the nylon muscle's actuated robotic finger structure.

$$\tau_3 = d_{31}\ddot{q}_1 + d_{32}\ddot{q}_2 + d_{33}\ddot{q}_3 + C_{113}\dot{q}_1^2 + C_{223}\dot{q}_2^2 + C_{333}\dot{q}_3^2 + (C_{213} + C_{123})\dot{q}_1\dot{q}_2$$
$$+ (C_{313} + C_{133})\dot{q}_3\dot{q}_1 + (C_{323} + C_{233})\dot{q}_2\dot{q}_3 + \varphi_1 + \tau_{d3}.$$

$$(9c)$$

Here we have the angular acceleration, $\ddot{q}$, angular velocity, $\dot{q}$, angular displacement, q, and the Coriolis components of acceleration, C_{ijk}, as well as the derivatives of potential erms, φ_k, including gravity

and spring stiffness (K), torque of the link k, τ_k, and the inertia matrix, d_{kj}.

Simulink® model used for numerical simulations and the complete derivation of Eq. (9) may be found in Ref. [36]. All of the inertia matrix's non-diagonal terms have been omitted from the model, including Coriolis terms due to insignificant effect. In both human and artificial finger joints, damping helps regulate oscillations. An additional
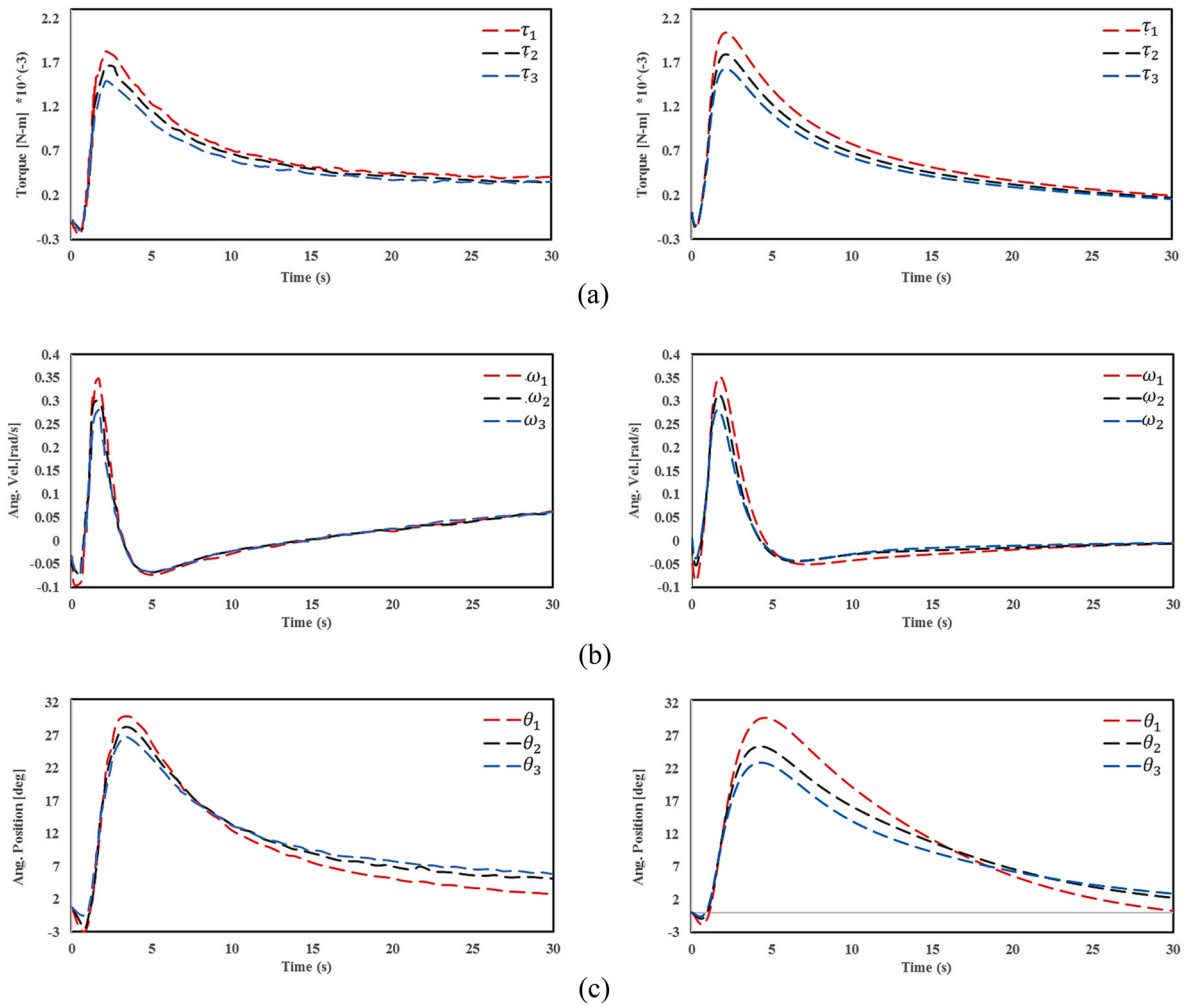
Fig. 5. The comparison of the (a) joint torques, (b) velocity, and (c) position angles for Saharan et al. [36] (left) and the present work (right).

Table 3
Spiral spring specifications with ABS and Nylon.

3D-printed spring joint	E/GPa	t/mm	K/N.m.deg^{-1}	L/mm
ABS, h = 0.4 mm	1.607	0.4	1.71×10^{-04}	(20 × pi)
ABS, h = 0.6 mm		0.6	8.68×10^{-04}	
ABS, h = 0.8 mm		0.8	2.74×10^{-03}	
Nylon, h = 0.4 mm	0.793	0.4	8.55×10^{-05}	
Nylon, h = 0.6 mm		0.6	4.34×10^{-04}	
Nylon, h = 0.8 mm		0.8	1.37×10^{-03}	

damping component ($\tau_{di} = c_d\, q_i$ (I = 1, 2, 3)) has been introduced in Eq. (9), which is related to the link's rotational velocity, q_i. Lewis et al. proposed a similar adjustment to the dynamic equation [38].

The torques at joints could be calculated by assuming the TCP actuator's output torque is distributed to each of the three joints mentioned above as given in Eq. (10)

$$\tau_3 = \gamma\tau \quad , \quad \tau_2 = \beta\tau \quad , \quad \tau_1 = \alpha\tau \quad , \quad \tau = Fe \tag{10}$$

where τ_1 = MCP joint, τ_2 = PIP joint, and τ_3 = DIP joint, the force created by the TCP actuator, F, the space between the tendon and the joint is measured, e, and α, β, and γ are the torque shares at each joint. Depending on the finger's design and setup, these characteristics may be determined. A set of assumptions, similar to those in Refs. [39,40], was utilized to calculate the torque imparted to each joint. It was necessary to find all three angles, α, β, and γ, to match the experimental measurements in order to get an initial estimate of the simulated values with

assuming α = β = γ = 1, and then to adjust those initial estimates until they all agreed with the experimental measurements. Finally, the final values were 0.25, 0.22, and 0.20, respectively, which were utilized throughout this work.

Eq. (11), which is a more generic definition of kinetic energy, is written as Eq (12). The inertias are transformed to the inertial frame of reference using a rotation matrix (q) that correlates each linkage [41].

$$K = \frac{1}{2}m_i v_i^T v_i + \frac{1}{2}w_i^T I w_i \tag{11}$$

$$K = \frac{1}{2}\dot{q}^T \sum_{i=1}^{n}[m_i J_{vi}(q)^T J_{vi}(q) + J_{vi}(q)^T R_i(q) I_i R_i(q)^T J_{wi}(q)]\dot{q} \tag{12}$$

The short version of total kinetic energy is:

$$K = \frac{1}{2}\dot{q}^T D(q)\dot{q} \tag{13}$$

The finger links inertia matrix is given by D as:

$$D = \frac{1}{2}\dot{q}^T \sum_{i=1}^{n}[m_i J_{vi}(q)^T J_{vi}(q) + J_{wi}(q)^T R_i(q) I_i R_i(q)^T J_{wi}(q)] \tag{14}$$

Below are the inertia matrix components of Eq. (9):
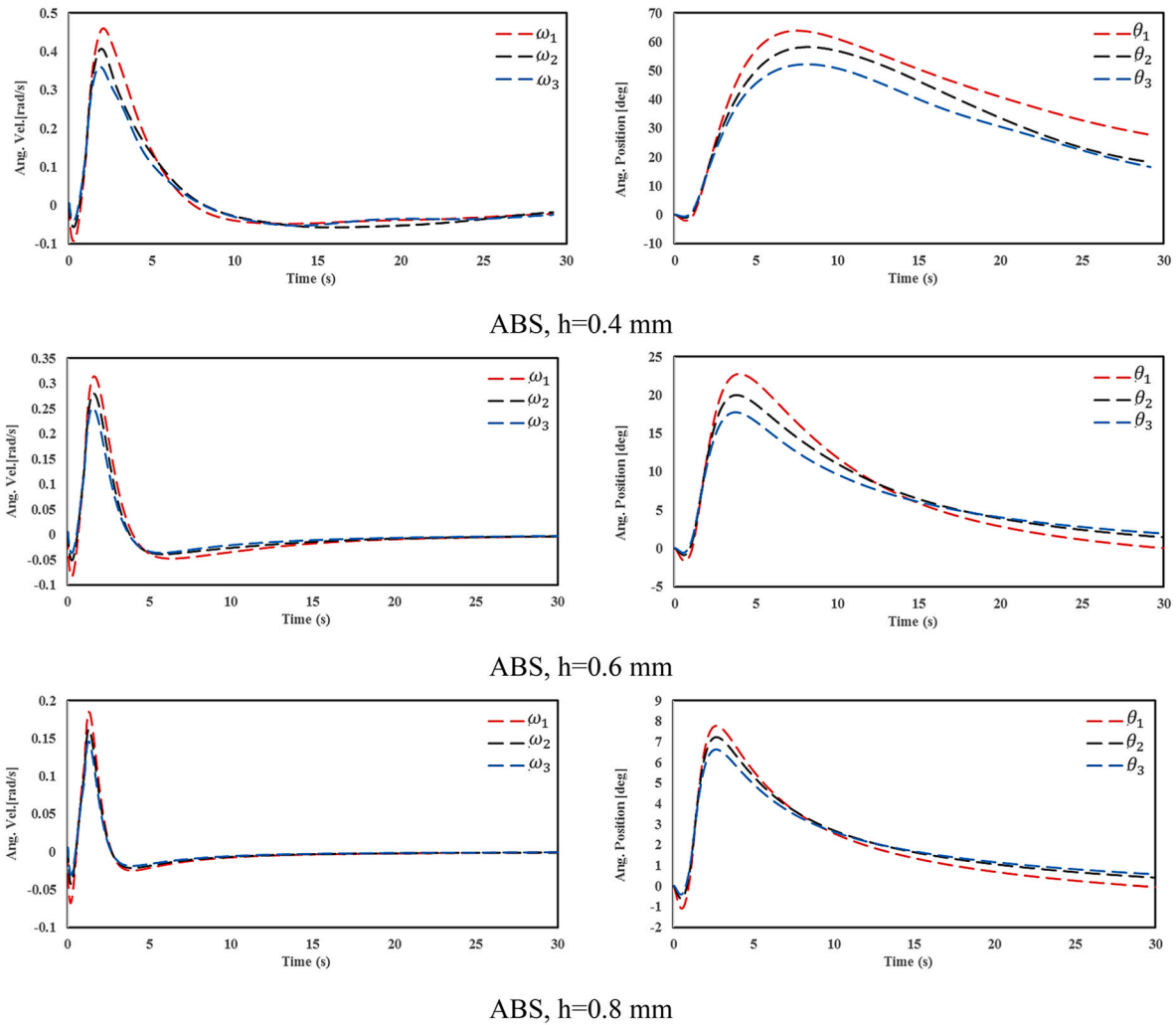
Fig. 6. The joint velocity (left) and position angles (right) results for the ABS and Nylon (h = 0.4, 0.6, and 0.8.).

$$\begin{cases} d_{11} = m_1 l_{c1}^2 + m_2\{l_1^2 + l_{c2}^2 + 2l_1 l_{C2}\cos q_2\} + m_3\{l_1^2 + l_2^2 + l_{c3}^2 + 2l_1 l_2 \cos q_2 \\ \quad +2l_2 l_{c3}\cos q_3 + l_{c3}\cos(q_2+q_3)\} + I_1 + I_2 + I_3 \\ d_{12} = d_{21} = m_2\{l_{c2}^2 + l_1 l_{C2}\cos q_2\} + m_3\{l_2^2 + l_{c3}^2 + 2l_2 l_{c3}\cos q_3 \\ \quad +l_1 l_2 \cos q_2 + l_1 l_{c3}\cos(q_2+q_3)\} + I_2 + I_3 \\ d_{13} = d_{31} = m_3\{l_{c3}^2 + l_1 l_{c3}\cos(q_2+q_3) + l_2 l_{c3}\cos q_3\} + I_3 \\ d_{23} = d_{32} = m_3\{l_{c3}^2 + l_2 l_{c3}\cos q_3\} + I_3 \\ d_{22} = m_3\{l_2^2 + l_{c3}^2 + 2l_2 l_{c3}\cos q_3\} + m_2 l_{c2}^2 + I_2 + I_3 \\ d_{33} = m_3 l_{c3}^2 + I_3 \end{cases}$$

(15)

For each link, l_{Ci} is the position of the gravitational center, assuming downward. Simulink® is used to model these components. Gravitational potential energy, P_g, for the robot's finger is shown in the following:

$$P_g = P_1 + P_2 + P_3 \tag{16}$$

where

$$P_1 = m_1 g l_{c1} sin q_1 \tag{17}$$

$$P_2 = m_2 g(l_1 sin q_1 + l_{c2}\sin(q_1+q_2)) \tag{18}$$

$$P_3 = m_3 g(l_1 sin q_1 + l_2 \sin(q_1+q_2) + l_{c3}\sin(q_1+q_2+q_3)) \tag{19}$$

Torsional springs Kt_i ($i =$1, 2, 3) provide the return motion in this robotic finger. The spring-induced elastic potential energy P_e may be expressed as:

$$P_e = \frac{1}{2}\left(Kt_1\, q_1^2 + Kt_2\, q_2^2 + Kt_3\, q_3^2\right) \tag{20}$$

As a result, P is equal to

$$P = (ml_{c1} + m_2 l_1 + m_3 l_1)g \sin q_1 + (ml_{c1} + m_2 l_1 + m_3 l_1)g \sin(q_1+q_2+) \\ + m_3 g l_{c3}\sin(q_1+q_2+q_3) + \frac{1}{2}\left(Kt_1 q_1^2 + Kt_2 q_2^2 + Kt_3 q_3^2\right) \tag{21}$$

Consequently, energy derivative functions are defined as:

$$\varnothing_1 = \frac{\partial P}{\partial q_1} \quad \varnothing_2 = \frac{\partial P}{\partial q_2} \quad \varnothing_3 = \frac{\partial P}{\partial q_3} \tag{22}$$

Table 2 lists all the simulation parameters.

2.3. Simulink model for the finger joint

A Simulink model was built using the equations from the previous section (Fig. 4). The three links are represented by the three major blocks in this design. In Fig. 3, the torque on the left side of each block represents the input. The simulation outputs are in green. As shown in Fig. 3, there are several sub-blocks included in the design. The Simulink

Nylon, h=0.4 mm

Nylon, h=0.6 mm

Nylon, h=0.8 mm
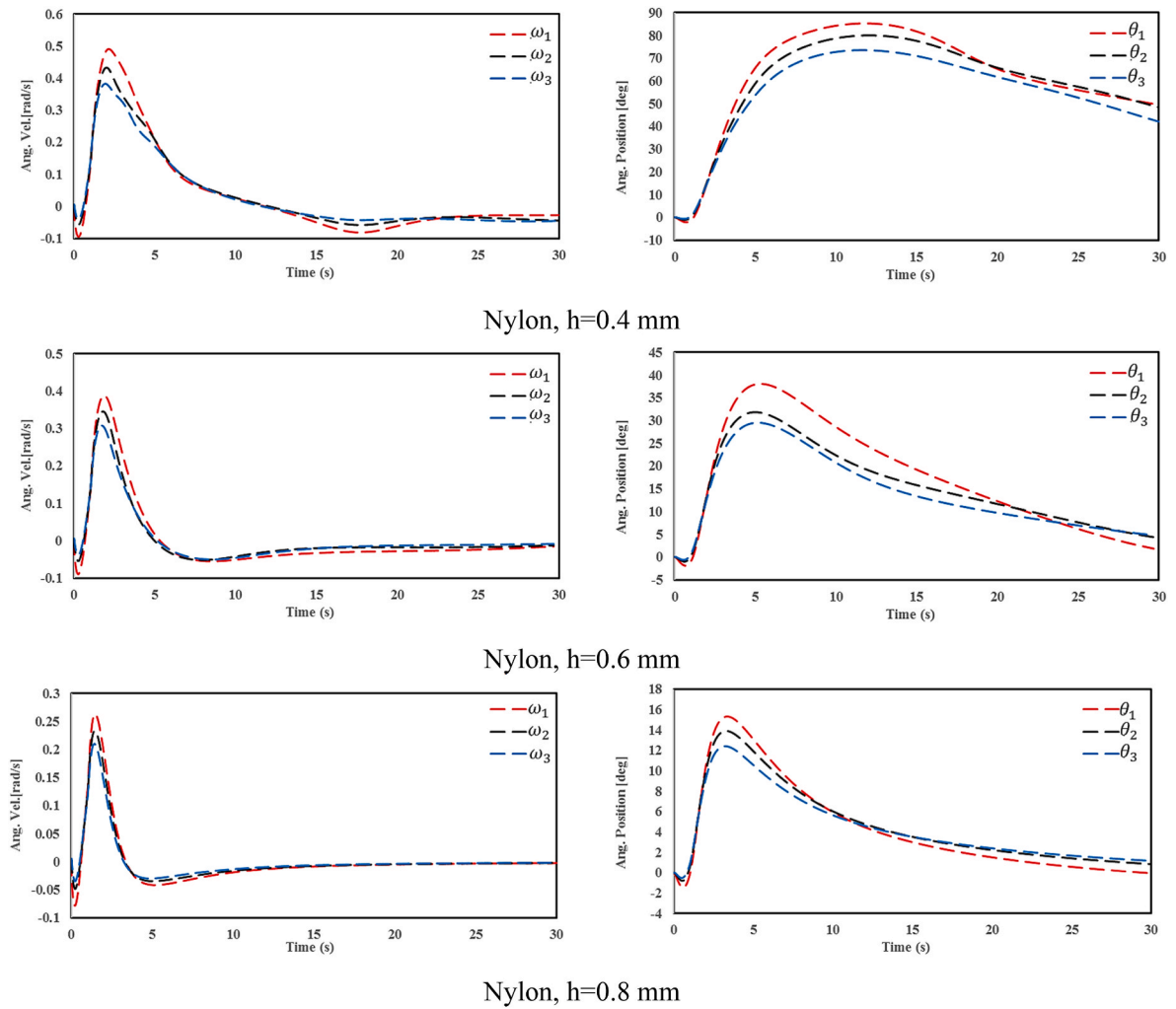
Fig. 6. (*continued*).
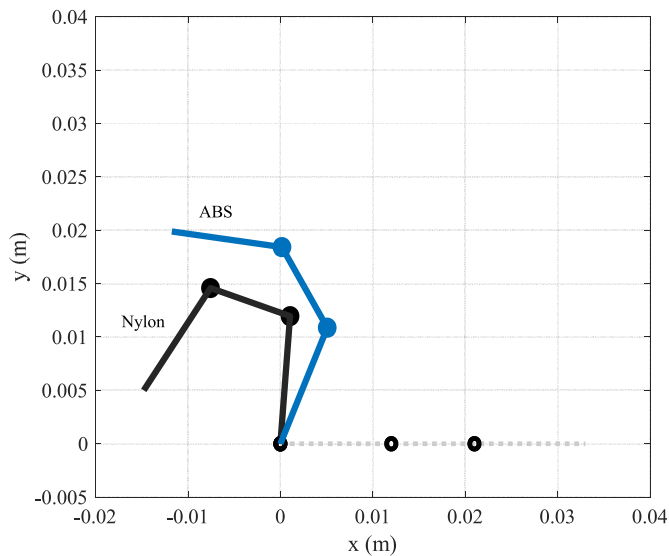
Fig. 7. Comparison of the maximum deflection the finger endpoint reaches for different stiffness 3D-printed joints.

blocks and tools shown here may be utilized to simulate the dynamic motion of fingers that are activated by different inputs.

3. Results and discussions

3.1. Validation of the results

According to Ref. [36] and the electrothermal relation presented in (6a), electrical power heats up TCP muscle and makes it contract, and this causes the finger to bend at an angle. The electric current is typically 2.5 amps (3.4 W/cm) when normalized by length. Fig. 5 presents a validation of the results of this work with those in Ref. [36], In this case, two sorts of simulations were conducted here. The first simulation was run using the experimentally measured load cell force of the TCP muscle as the input, referred to it as "force input-based simulation" (FIS). The torque felt by the finger was calculated by multiplying the force data by the offset value e (Fig. 3 (a), left). It was then used to calculate angular positions and angular velocities of the finger joints using Eqs. 9 and 10. Two transfer functions are coupled in sequence to produce the second simulation for electro-thermal and thermo-mechanical models obtained from the system identification. They provided the experimentally observed input power and measured output force that was multiplied by an offset distance to obtain torque. Also, Fig. 5 shows the average error of the current model compared with the earlier results Saharan et al. [36]. The average errors obtained for the ω, θ, and τ equal to 2.15%, 8.18% and 9.66%, respectively. That's why the average error obtained is

below 10%.

3.2. The results of the present study by changing the stiffness coefficient K spring

To design the helical spring, the formula described in Section 2.1 was used with the specifications of ABS and nylon 3D printing, the result of which is shown in Table 3. This data is used in the Simulink® model to calculate finger joint parameters. The results for ABS and nylon, h = 0.4, 0.6, and 0.8 mm, are shown in Fig. 6. By increasing the values of h (0.4, 0.6, and 0.8) in ABS joint both θ and ω decrease. This implies the significance of 3D printed joints in the stiffness control of the finger mechanism. The same is true for nylon. As, the values of h (0.4, 0.6, and 0.8) have a direct effect on the variations of θ and ω. A comparison of the results obtained for ABS and nylon in Fig. 7 with reference to Fig. 2. b. It shows that the maximum deviation of the end point of the finger is different for different joint stiffness made via different 3D printing materials. The maximum deviation of the finger end point for nylon material is greater than for ABS, which suggests the use of nylon material in soft robots.

4. Conclusions

This paper presented a method of integrating additive manufacturing into tendon-driven soft robotic finger actuated by polymeric muscles. An electro-thermal soft actuator mechanism is introduced, including the non-assembly 3D-printed compliant joint for articulation of a robotic finger. The simulation analysis was done to find out how the properties of the electro thermal muscle and the spiral spring joint affect the movement of the finger. The robotic finger is actuated by twisted and coiled polymer (TCP) in this study. Such actuators are opted due to their high performance and the available experimental data, which well-represent artificial muscles made from smart materials. Euler–Lagrangian methods for modeling, simulating, and testing the results were applied. Simulink® models based on the equation set were also developed to conduct numerical simulations.

The simulation results were validated based on the experimental data for the system. Then, the three-dimensional (3D)-printed spiral spring joints with defined stiffness were designed, fabricated, and simulated using the validated model. A sensitivity analysis of the tendon-driven muscle using additively manufactured joints with variable stiffness was performed. It was shown that additive manufacturing could positively contribute towards customization and scalability in joint design with desired stiffness.

The soft gripper models using actuators such as SMA or SMP may benefit from the technique shown in this paper. Next, the findings of this dynamic modeling would be used to create closed-loop controller for each of the fingers. The results revealed further understanding of the 3D-printed spiral spring joints' effects in the tendon-driven structures The mechanism proposed could be changed and used in the 4D printing, medical and industrial sectors with a wide range of shapes and objects.

Credit author statement

Ali Zolfagharian: Conceptualization, Funding acquisition, Formal analysis, Investigation, Validation, Writing – original draft. **Mohammad Lakhi**: Software, Methodology, Investigation, Writing – original draft, Validation. **Sadegh Ranjbar**: Software, Methodology, Validation, Project administration. **Yonas Tadesse**: Methodology, Investigation, Validation, Writing-review & editing. **Mahdi Bodaghi**: Methodology, Investigation, Project administration, Writing-review & editing. We confirm that the manuscript has been read and approved by all named authors. We confirm that the order of authors listed in the manuscript has been approved by all named authors.

Declaration of competing interest

The authors declare that they have no known competing financial interests or personal relationships that could have appeared to influence the work reported in this paper.

References

[1] M.F.M.D.J. Mendoza, A.M. López, Adaptive gripper controlled with linear micro actuator for correct fastening of objects of variant forms, Int. J. Mech. Eng. Robot. Res. 9 (4) (2020).

[2] Z. Wang, Y. Torigoe, S. Hirai, A prestressed soft gripper: design, modeling, fabrication, and tests for food handling, IEEE Rob. Autom. Lett. 2 (4) (2017) 1909–1916.

[3] C. Liang, et al., Design and control of a novel asymmetrical piezoelectric actuated microgripper for micromanipulation, Sensor Actuator Phys. 269 (2018) 227–237.

[4] J.S. Cuellar, et al., Ten guidelines for the design of non-assembly mechanisms: the case of 3D-printed prosthetic hands, Proc. IME H J. Eng. Med. 232 (9) (2018) 962–971.

[5] B.C. Mac Murray, et al., Compliant buckled foam actuators and application in patient-specific direct cardiac compression, Soft Robot. 5 (1) (2018) 99–108.

[6] R. Noroozi, et al., Shape-adaptive metastructures with variable bandgap regions by 4D printing, Polymers 12 (3) (2020) 519.

[7] A. Zolfagharian, et al., 3D printed soft parallel actuator, Smart Mater. Struct. 27 (4) (2018), 045019.

[8] A.A. Amiri Moghadam, et al., Control-oriented modeling of a polymeric soft robot, Soft Robot. 3 (2) (2016) 82–97.

[9] C.-H. Liu, et al., A soft robotic gripper module with 3D printed compliant fingers for grasping fruits, in: 2018 IEEE/ASME International Conference on Advanced Intelligent Mechatronics (AIM), IEEE, 2018.

[10] R. Deimel, O. Brock, A novel type of compliant and underactuated robotic hand for dexterous grasping, Int. J. Robot Res. 35 (1–3) (2016) 161–185.

[11] M. Manti, et al., A bioinspired soft robotic gripper for adaptable and effective grasping, Soft Robot. 2 (3) (2015) 107–116.

[12] R.M. McKenzie, T.W. Barraclough, A.A. Stokes, Integrating soft robotics with the robot operating system: a hybrid pick and place arm, Front. Robot. AI 4 (2017) 39.

[13] N. Maqsood, M. Rimašauskas, Delamination observation occurred during the flexural bending in additively manufactured PLA-short carbon fiber filament reinforced with continuous carbon fiber composite, Res. Eng. 11 (2021), 100246.

[14] V. Iyer, et al., Wireless analytics for 3D printed objects, in: Proceedings of the 31st Annual ACM Symposium on User Interface Software and Technology, 2018.

[15] A. Zolfagharian, A. Kaynak, A. Kouzani, Closed-loop 4D-Printed Soft Robots, Materials & Design, 2019, 108411.

[16] M.S. Xavier, et al., 3D-printed omnidirectional soft pneumatic actuators: design, modeling and characterization, Sensor Actuator Phys. 332 (2021), 113199.

[17] D.S. Cheah, et al., Development of 4D-printed shape memory polymer large-stroke XY micropositioning stages, J. Micromech. Microeng. 32 (6) (2022), 065006.

[18] M. Bodaghi, A. Damanpack, W. Liao, Adaptive metamaterials by functionally graded 4D printing, Mater. Des. 135 (2017) 26–36.

[19] M. Bodaghi, A. Damanpack, W. Liao, Self-expanding/shrinking structures by 4D printing, Smart Mater. Struct. 25 (10) (2016), 105034.

[20] C.-H. Liu, et al., Topology and size–shape optimization of an adaptive compliant gripper with high mechanical advantage for grasping irregular objects, Robotica 37 (8) (2019) 1383–1400.

[21] F. Ullrich, et al., Magnetically actuated and guided milli-gripper for medical applications, in: 2015 IEEE International Conference on Robotics and Automation (ICRA), IEEE, 2015.

[22] S. Song, et al., Toward tradeoff between impact force reduction and maximum safe speed: dynamic parameter optimization of variable stiffness robots, J. Mech. Robot. 12 (5) (2020).

[23] Z. Qaiser, S. Johnson, Generalized Spiral Spring (GSS): a bioinspired tunable stiffness mechanism (TSM) for linear response with high resolution, J. Mech. Robot. (2019) 1–32.

[24] S. Marinković, et al., Cochlea and other spiral forms in nature and art, Am. J. Otolaryngol. 33 (1) (2012) 80–87.

[25] V. Iyer, J. Chan, S. Gollakota, 3D printing wireless connected objects, ACM Trans. Graph. 36 (6) (2017) 1–13.

[26] Y. Yang, E.S. Jeon, D.H. Park, Optimization of design parameters of spiral spring for active headrest deployment, in: MATEC Web of Conferences, EDP Sciences, 2018.

[27] G. Carpino, et al., A novel compact torsional spring for series elastic actuators for assistive wearable robots, J. Mech. Des. 134 (12) (2012).

[28] H. Liu, et al., Design and vibration suppression control of a modular elastic joint, Sensors 18 (6) (2018) 1869.

[29] J. Yan, et al., A human-inspired soft finger with dual-mode morphing enabled by variable stiffness mechanism, Soft Robot. 9 (2) (2022) 399–411.

[30] A. Zolfagharian, et al., A Bioinspired Compliant 3D-Printed Soft Gripper, Soft Robotics, 2021.

[31] D. Dragone, et al., Design, computational modelling and experimental characterization of bistable hybrid soft actuators for a controllable-compliance joint of an exoskeleton rehabilitation robot, in: Actuators, MDPI, 2022.

[32] S.B. Balani, et al., Processes and materials used for direct writing technologies: a review, Res. Eng. 11 (2021), 100257.

[33] U. Scarcia, et al., Optimal design of 3d printed spiral torsion springs, in: Smart Materials, Adaptive Structures and Intelligent Systems, American Society of Mechanical Engineers, 2016.

[34] D. Handbook, Associated Spring-Barnes Group, Bristol, CT, 1981.

[35] J.-S. Chen, I.-S. Chen, Deformation and vibration of a spiral spring, Int. J. Solid Struct. 64 (2015) 166–175.

[36] L. Saharan, L. Wu, Y. Tadesse, Modeling and Simulation of Robotic Finger Powered by Nylon Artificial Muscles-Equations with Simulink Model, 2019 arXiv preprint arXiv:1901.09486.

[37] M.W. Spong, S. Hutchinson, M. Vidyasagar, Robot modeling and control, Ind. Robot: Int. J., 2006.

[38] F.L. Lewis, D.M. Dawson, C.T. Abdallah, Robot Manipulator Control: Theory and Practice, CRC Press, 2003.

[39] L. Zollo, et al., Biomechatronic design and control of an anthropomorphic artificial hand for prosthetic and robotic applications, IEEE/ASME Trans. Mechatron. 12 (4) (2007) 418–429.

[40] M.C. Carrozza, et al., The SPRING hand: development of a self-adaptive prosthesis for restoring natural grasping, Aut. Robots 16 (2) (2004) 125–141.

[41] M.W. Spong, S. Hutchinson, M. Vidyasagar, Robot Modeling and Control, vol. 3, wiley, New York, 2006.